Peer-reviewed version available at Geosciences 2018, 8, 445; doi:10.3390/geosciences8120445

# Phase evolution and textural changes during the direct conversion and storage of $CO_2$ to produce calcium carbonate from calcium hydroxide

*Meishen Liu and Greeshma Gadikota*[1,*]

[1]Department of Civil and Environmental Engineering

Environmental Chemistry and Technology Program, Geological Engineering Program

Grainger Institute for Engineering

University of Wisconsin-Madison, Madison, WI 53706

[1] Corresponding Author. Phone: +1 608-262-0365. E-mail: gadikota@wisc.edu

## Abstract

The increasing use of energy resources recovered from the subsurface environments and the resulting carbon imbalance in the environment has motivated the need to develop thermodynamically downhill pathways to convert and store $CO_2$ as water insoluble calcium or magnesium carbonates. While previous studies extensively explored aqueous routes to produce calcium and magnesium carbonates from $CO_2$, there has been a limited scientific understanding of the phase evolution and textural changes during the direct gas-solid conversion routes to produce calcium carbonate from calcium hydroxide, which is one of the abundant constituents of alkaline industrial residues. With increasing interest in developing integrated pathways for capturing, converting and storing $CO_2$ from dilute flue gases, understanding the compositions of the product phases as they evolve is essential for evaluating the efficacy of a given processing route. Therefore, in this study, we investigate the phase evolution and the corresponding textural changes as calcium hydroxide is converted to calcium carbonate under the continuous flow of $CO_2$ at an ambient pressure of 1 atm and on heating continuously from 30 °C to 500 °C using *in-operando* wide angle X-ray scattering (WAXS), small angle X-ray scattering (SAXS), and ultra-small angle X-ray scattering (USAXS) measurements.


***Keywords:*** ultra-small angle X-ray scattering (USAXS), small angle X-ray scattering (SAXS), wide angle X-ray scattering (WAXS), calcium hydroxide, calcium carbonate, carbon capture, utilization, and storage; carbon mineralization.

Peer-reviewed version available at Geosciences 2018, 8, 445; doi:10.3390/geosciences8120445

## 1. Introduction

One of the emerging challenges in sustainable energy production is the development of integrated pathways for carbon dioxide capture, utilization and storage (CCUS). With $CO_2$ concentrations increasing from about 280 ppm before the industrial age to over 400 ppm now, the need for CCUS technologies is unprecedented [1–4]. The transition to a low carbon economy will require us to develop a portfolio of technologies for capturing, utilizing and storing $CO_2$ at the gigaton scale [5]. Carbon mineralization is one approach which involves the accelerated conversion and storage of $CO_2$ as water insoluble calcium and magnesium carbonate via thermodynamically downhill routes [6–12]. Various routes including gas-solid and gas-liquid-solid reaction routes have been explored to accelerate the conversion of $CO_2$ to calcium and magnesium carbonates [13–15]. While gas-solid reaction routes are easier to implement, the kinetics of $CO_2$ conversion to calcium and magnesium carbonates may be slower. However, with increasing interest in directly using dilute concentrations of $CO_2$ representative of flue gas concentrations or atmospheric CO2 concentrations, the need to understand the phase transitions and the textural changes in sorbents such as calcium hydroxide as it is converted to calcium carbonate provides important insights into the composition of these materials for potential use.

One of the key motivations for investigating the phase transitions and textural changes of calcium hydroxide during carbon mineralization is the abundance of these materials in alkaline industrial residues such as carbide slag [16]. Carbide slag is one of the by-products of the hydrolysis of calcium carbide ($CaC_2$), a reaction generating ethylene, polyvinyl chloride (PVC) and other products in the industry [17]. Significant quantities of carbide slag are generated around the world. For example, in China, 70% of ethyne ($C_2H_2$), a raw material of polyvinyl chloride (PVC), is generated from calcium carbide. About one ton of PVC results in the production of 1.5–

Peer-reviewed version available at Geosciences 2018, 8, 445; doi:10.3390/geosciences8120445

1.9 tons of carbide slag in an industrial plant [17,18]. However, treating carbide slag in an economical manner has been a challenge. While landfilling these materials has been proposed, carbide slag is caustic and corrosive, which increases the risk of environmental contamination. Another approach to utilize carbide slag is to use it to produce cement [18,19]. Recently, a calcium looping process (CLP) was proposed to integrate carbide slag disposal and $CO_2$ capture [20–22]. In this approach, carbide slag, recovered from energy-intensive industrial plants, could be used to capture $CO_2$, which is generated by industrial plants, and then used as raw materials to produce cement [23–25].

Previous studies discussing $CO_2$ capture with carbide slag or modified carbide slag reported that carbonate conversions up to 28% could be reached after 100 calcination/carbonation cycles in the optimal temperature range of 650–700 °C [17]. Modified sorbents produced from carbide slag using reagents such as aluminum nitrate hydrate and glycerol water solution and propionic acid has higher $CO_2$ capture capacity compared to untreated slag. While these studies focused on enhancing the conversion of carbide slag, there was a limited fundamental understanding of the phase transitions and textural behavior of the key constituents of carbide slag such as calcium hydroxide [26,27].

In this paper, the evolution of calcium carbonate phases from calcium hydroxide and the corresponding changes in the roughness of the pore-solid interface are investigated using *in-operando* synchrotron ultra-small, small, and wide angle X-ray scattering (USAXS/SAXS/WAXS) measurements [6,8,10,11,28–32]. The wide angle X-ray scattering measurements provide unambiguous insights into the structural changes, while ultra-small and small angle X-ray scattering measurements reveal the changes in the textures of the pore-solid interface during the carbon mineralization of calcium hydroxide to produce calcium carbonate. Calcium hydroxide is

Peer-reviewed version available at Geosciences 2018, 8, 445; doi:10.3390/geosciences8120445

continuously reacted with $CO_2$ flowing at 1 atm while being heated from 30 °C to 500 °C in a capillary reaction cell as the multi-scale X-ray scattering measurements were taken. While recent efforts by Benedetti, Ilavsky and co-workers relate the reactivity of calcium oxide with $CO_2$ during carbonation and calcination cycles using microstructural modeling of the USAXS [33], in this study, we systematically track the structural evolution of calcium carbonate as it is formed from calcium hydroxide.

## 2. Experimental Methods

### 2.1 Materials and Methods

Calcium hydroxide powder procured from Himedia Laboratories (West Chester, PA, USA) was placed in a quartz capillary with an internal diameter of 1.3 mm and thickness of 0.2 mm (Friedrich & Dimmock Inc., Millville, NJ, USA) and loaded into a capillary cell holder [34]. Glass wool was placed at both ends of the capillary to hold the powder in place. $CO_2$ was continuously supplied at a flow rate of 10 mL/min. Temperatures in the range of 29 °C to 502 °C were investigated and the ramp rate was set to 4.73 °C /min. The surface area and cumulative pore volume of $Ca(OH)_2$ used in this experiment is 8.65 ($\pm$0.82) $m^2/g$ and 0.0134 ($\pm$0.0017) mL/g, respectively. The pore size distribution of calcium hydroxide is shown in **Figure 1**.

### 2.2 USAXS/SAXS/WAXS measurements

The multi-scale X-ray scattering measurements were performed at Sector 9-ID at the Advanced Photon Source (APS) in Argonne National Laboratory (ANL), Argonne, IL [35]36]. Temporal uncertainties in the collected data were reduced with rapid acquisition times which were set to 90 s, 30 s, and 30 s for USAXS, SAXS, and WAXS, respectively. The total X-ray flux, energy and corresponding wavelength were $10^{-13}$ photon $s^{-1}$, 21.0 keV, and 0.59 Å, respectively. SAXS and WAXS measurements were calibrated using silver behenate and the NIST standard

reference material, SRM 640d (Si), respectively [37]. Data analyses were performed in the Irena and Nika software packages embedded in *IgorPro* (Wavemetrics, Lake Oswego, OR) [38,39].

## 3. Results and Discussion

### 3.1 Phase transformations during the carbon mineralization of calcium hydroxide

The changes in the structure of calcium hydroxide were determined from the wide angle X-ray scattering data. The characteristic peak of calcium hydroxide which corresponds to the (1 0 0) reflection at $q$ = 2.024 Å$^{-1}$ undergoes significant changes with continuous $CO_2$ flow as the temperature increases (**Figure 2**) [40]. The shift in the characteristic peak to lower $q$ or larger $d$ values corresponds to thermal expansion, as reported in previous studies [10,28,41]. Tracking the changes in the integrated intensity of calcium hydroxide peak yields important insights into the onset of carbon mineralization behavior. The relative integrated intensity of calcium hydroxide as it reacts with $CO_2$ and with increasing temperature is shown in **Figure 2(b)**. As the reaction temperature is increased to 400 °C, the peak intensity is reduced to 60% of the original value at ambient temperature (**Figure 2(b)**). A steeper reduction in the integrated peak intensity to 15% of the original value at ambient temperature is noted as the reaction temperature increases to 500 °C. These observations were consistent the changes in the characteristic (0 0 1) reflection of calcium hydroxide at $q$ = 1.28 Å$^{-1}$ (**Figure S1 (a) and (b)**). The relative integrated intensity of this peak decreases from 80 % at 400 °C to 30 % at 500 °C, which provides additional validation of major structural changes of calcium hydroxide to produce calcium carbonate. The disappearance of the characteristic peaks of calcium hydroxide as it is reacted with $CO_2$ is consistent with previous studies [17,42,43].

The disappearance of the calcium hydroxide peaks corresponds to the onset of calcium carbonate peaks. The onset of three different phases of calcium hydroxide: aragonite, vaterite and

calcite is noted during the carbon mineralization process. The characteristic peaks of calcite (0 1 2) at $q$ = 1.63 Å$^{-1}$, vaterite (1 1 0) at $q$ = 3.02 Å$^{-1}$, and aragonite (2 1 0) at $q$ = 2.53 Å$^{-1}$ in WAXS regime, all start to emerge at 300 °C. These data suggest that all types of $CaCO_3$ form at the same time, instead of transforming from one structure to another [44–46]. The integrated peak intensities show that the growth of the calcium carbonate phases is significantly enhanced as the temperature increases above 400 °C (**Figure 3**). These observations are consistent with previous papers [42]. It was also interesting to note that the formation of calcium carbonate phases did not level off on heating to 500 °C suggesting that less than 100% conversion of calcium hydroxide to calcium carbonate was achieved (**Figure 3**). A comparison of the wide angle X-ray scattering data at 30 °C and 497 °C suggests that the amount of calcium hydroxide present in the sample reacted at 497 °C may be too small to be detected compared to the abundance of the calcium carbonate present. It was also interesting to note the formation of denser calcium carbonate phases compared to the less dense calcium hydroxide material. The densities of calcite, vaterite, and aragonite are 2.71, 2.65, 2.94 g/cm$^3$ respectively [47]. In comparison, the density of calcium hydroxide is 2.21 g/cm$^3$. The influence of forming more dense phases on the textural properties of the end product are discussed in the following section.

### 3.2 Evolution of the pore-solid interface during the carbon mineralization of calcium hydroxide

As discussed in the previous section, the changes in the density and shape of the product phases during carbon mineralization may potentially impact the morphology of the material as the reaction proceeds. Insights into the morphological changes of calcium hydroxide as it is converted to calcium carbonate are obtained from the combined Ultra-Small and Small Angle X-Ray Scattering (USAXS/SAXS) data. The combined USAXS/SAXS data of calcium hydroxide during

carbon mineralization is represented at temperatures in the range of 29-300 °C and 325-502 °C in **Figure 4 (a)** and **Figure 4 (b)**, respectively.

The intensity of the USAXS/SAXS data did not change significantly on heating from ambient temperature to 300 °C as shown in **Figure 4(a)**. The small reduction in the intensity of the scattering data at q in the range of 0.1 to 2 $Å^{-1}$ suggests a coarsening in the morphology of the calcium hydroxide. Significant reduction in the scattering intensity, particularly in the range of 0.01 – 0.1 $Å^{-1}$ is noted. This reduction corresponds to the onset and growth of denser calcium carbonate phases and depletion of calcium hydroxide (**Figure 4(b)**). These data suggest that the newly formed $CaCO_3$ phases may occupy the pores of calcium hydroxide resulting in a lower scattering intensities.

Determination of the Porod slopes in the q-range of 0.001-0.01 $Å^{-1}$ and 0.01-0.1 $Å^{-1}$ provided detailed insights into the pore-solid interface. Previous literature reports the fractal character of porous materials such as calcium hydroxide, (surface fractal dimension Ds = 2.0 [48]) calcium carbonate, (surface fractal dimension, $D_s$ = 1.7665 [49]) cementitious materials (The fractal dimension found was universally 1.25 in pore boundary fractal terms [50]), shales (surface fractal dimension is 3.4 [51]) using scattering techniques. In this study, the fractality of the microstructure is probed in the *q* regions of 0.001-0.01 $Å^{-1}$ and 0.01-0.1 $Å^{-1}$ using the universal porod slope model. The porod slope is calculated based on the relationships shown below, where *I (q)* represents the scattering intensity and the *n* represents the porod slope.

$$I\,(q) = \frac{A}{q^n} + B \qquad \text{(Equation 1)}$$

$$\log_{10}[I\,(q) - B] = \log_{10} A - n \log_{10} q \qquad \text{(Equation 2)}$$

Peer-reviewed version available at Geosciences 2018, 8, 445; doi:10.3390/geosciences8120445

The growth of denser and crystalline calcium carbonate phases results in increasingly smoother pore-solid interfaces in the high *q* and low *q* regimes as shown in **Figure 5**. Porod slope in the low *q* regime is in the range of 2-3, which is indicative of a branched or mass fractal morphology at larger length scales. Porod slopes in the high *q* regime are in the range of 3-4, which is indicative of a surface fractal morphology or rough pore-solid interfaces. The changes in the porod slopes were much larger in the high *q* regime as opposed to in the low *q* regime suggesting that the morphologies at the larger length scales are branched while the local microstructures are characterized by surface fractal morphologies. These data also suggest that the changes in the local microstructure are much larger compared to the changes in the bulk morphology. The increase in the porod slope from 3.3 to 3.6 in the high *q* regime of the USAXS/SAXS data suggests that the relative smoothness of the pore-solid interface may be enhanced during the growth of the calcium carbonate phases. These observations are consistent with previously observed studies that report smoother pore-solid interfaces resulting from the growth of denser, crystalline phases [10,50].

## 4. Conclusions

In this study, we report the phase transitions and the textural changes as calcium hydroxide, one of the significant components of alkaline industrial residues, is converted to calcium carbonate using *in-operando* Ultra-Small, Small, and Wide Angle X-Ray Scattering (USAXS/SAXS/WAXS) measurements. The onset of calcium carbonate formation is noted at 300 °C and the progressive growth of these phases is noted as the temperature increases to 500 °C. The simultaneous onset of three different calcium carbonate phases identified as calcite, vaterite, and aragonite are reported. Textural changes as calcium hydroxide is converted to calcium carbonate are noted. The pore-solid interface in the high *q* regime in the range of 0.01-0.1 $Å^{-1}$ is representative of a surface fractal morphology. Reduced roughness of the pore-solid interface is noted due to the formation of denser

and crystalline phases of calcium carbonate. These data suggest that connecting the phase transitions and the morphologies of alkaline-bearing materials as they are converted to their respective carbonates has important implications for process scale considerations such as the temperature conditions that yield optimal composition and morphology of the desired end-products.

**Acknowledgements**

The authors gratefully acknowledge the Wisconsin Alumni Research Foundation and the College of Engineering at the University of Wisconsin, Madison. A special thanks to Dr. Jan Ilavsky and Dr. Ivan Kuzmenko, X-ray Science Division, Argonne National Laboratory, for providing experimental support for the combined USAXS/SAXS/WAXS measurements at the Advanced Photon Source. The use of the Advanced Photon Source, an Office of Science User Facility operated for the U.S. Department of Energy (DOE) Office of Science by Argonne National Laboratory, is supported by the U.S. DOE under Contract DE-AC02-06CH11357.

## References

1. Fauth, D. J.; Goldberg, P. M.; Knoer, J. P.; Soong, Y.; O'Connor, W. K.; Dahlin, D. C.; Nilsen, D. N.; Walters, R. P.; Lackner, K. S.; Ziock, H. J.; McKelvy, M. J.; Chen, Z. Y. Carbon dioxide storage as mineral carbonates. *ACS Div. Fuel Chem. Prepr.* **2000**, *45*, 708–711.
2. Lackner, K. S. Carbonate chemistry for sequestering fossil carbon. *Annu. Rev. Energy Environ.* **2002**, *27*, 193–232.
3. Seifritz, W. $CO_2$ disposal by means of silicates. *Nature* **1990**, *345*, 486–486.
4. Metz, B., IPCC special report on carbon dioxide capture and storage. Cambridge University Press, UK, **2005**.
5. Mission Innovation: Accelerating the clean energy revolution. Report of the Carbon Capture, Utilization and Storage Experts' Workshop. Houston, TX, September 26-28, **2017**.
6. Gadikota, G.; Matter, J.; Kelemen, P.; Park, A.-H. A. Chemical and morphological changes during olivine carbonation for $CO_2$ storage in the presence of NaCl and $NaHCO_3$. *Phys. Chem. Chem. Phys.* **2014**, *16*, 4679–4693.
7. Gadikota, G.; Swanson, E.; Zhao, H.; Park, A.-H. A. Experimental Design and Data Analysis for Accurate Estimation of Reaction Kinetics and Conversion for Carbon Mineralization. *Ind. Eng. Chem. Res.* **2014**, *53*, 6664-6676.
8. Gadikota, G.; Park, A.-H. A. Accelerated Carbonation of Ca- and Mg-Bearing Minerals and Industrial Wastes Using $CO_2$. In *Carbon Dioxide Utilisation: Closing the Carbon Cycle*; **2015**, 115–137.
9. Gadikota, G.; Fricker, K. J.; Jang, S.-H.; Park, A. H. A. Carbonated silicate minerals and industrial wastes as construction materials. In *Advances in $CO_2$ Capture, Sequestration, and*

*Conversion*, ACS Books, **2015**, 295-322.

10. Liu, M.; Gadikota, G. Chemo-morphological coupling during serpentine heat treatment for carbon mineralization. *Fuel* **2018**, *227*, 379–385.
11. Liu, M.; Gadikota, G. Integrated $CO_2$ capture, conversion and storage to produce calcium carbonate using an amine looping strategy. *Energy & Fuels* **2018**.
12. Power, I. M; Harrison, A. L.; Dipple, G. M.; Wilson, S. A.; Kelemen, P. B.; Hitch, M.; Southam, G. Carbon mineralization: from natural analogues to engineered systems. *Reviews in Mineralogy and Geochemistry*, **2013**, *77*, 305-360.
13. Sanna, A.; Hall, M. R.; Maroto-Valer, M. Post-processing pathways in carbon capture and storage by mineral carbonation (CCSM) towards the introduction of carbon neutral materials. *Energy Environ. Sci.* **2012**, *5*, 7781–7796.
14. Gerdemann, S. J.; O'Connor, W. K.; Dahlin, D. C.; Penner, L. R.; Rush, H. Ex situ aqueous mineral carbonation. *Environ. Sci. Technol.* **2007**, *41*, 2587–2593.
15. McKelvy, M. J.; Chizmeshya, A. V. G.; Diefenbacher, J.; Béarat, H.; Wolf, G. Exploration of the role of heat activation in enhancing serpentine carbon sequestration reactions. *Environ. Sci. Technol.* **2004**, *38*, 6897–6903.
16. Liu, W.; Yang, J.; Xiao, B. Review on treatment and utilization of bauxite residues in China. *Int. J. Miner. Process.* **2009**, *93*, 220–231.
17. Li, Y.; Sun, R.; Liu, C.; Liu, H.; Lu, C. $CO_2$ capture by carbide slag from chlor-alkali plant in calcination/carbonation cycles. *Int. J. Greenh. Gas Control* **2012**, *9*, 117–123.
18. Cheng, J.; Zhou, J.; Liu, J.; Cao, X.; Cen, K. Physicochemical characterizations and desulfurization properties in coal combustion of three calcium and sodium industrial wastes. *Energy and Fuels* **2009**, *23*, 2506–2516.

19. Cao, J.; Liu, F.; Lin, Q.; Zhang, Y. Hydrothermal synthesis of xonotlite from carbide slag. *Prog. Nat. Sci.* **2008**, *18*, 1147–1154.

20. Bobicki, E. R.; Liu, Q.; Xu, Z.; Zeng, H. Carbon capture and storage using alkaline industrial wastes. *Prog. Energy Combust. Sci.* **2012**, *38*, 302–320.

21. Li, B.; Duan, Y.; Luebke, D.; Morreale, B. Advances in $CO_2$ capture technology: A patent review. *Appl. Energy* **2013**, *102*, 1439–1447.

22. Blamey, J.; Anthony, E. J.; Wang, J.; Fennell, P. S. The calcium looping cycle for large-scale $CO_2$ capture. *Prog. Energy Combust. Sci.* **2010**, *36*, 260–279.

23. Liu, W.; An, H.; Qin, C.; Yin, J.; Wang, G.; Feng, B.; Xu, M. Performance enhancement of calcium oxide sorbents for cyclic $CO_2$ capture—A review. *Energy & Fuels* **2012**, *26*, 2751–2767.

24. Valverde, J. M. Ca-based synthetic materials with enhanced $CO_2$ capture efficiency. *J. Mater. Chem. A* **2013**, *1*, 447–468.

25. Manovic, V.; Anthony, E. J. Lime-based sorbents for high-temperature $CO_2$ capture-a review of sorbent modification methods. *Int. J. Environ. Res. Public Health* **2010**, *7*, 3129–3140.

26. Li, Y.; Su, M.; Xie, X.; Wu, S.; Liu, C. $CO_2$ capture performance of synthetic sorbent prepared from carbide slag and aluminum nitrate hydrate by combustion synthesis. *Appl. Energy* **2015**, *145*, 60–68.

27. Sun, R.; Li, Y.; Zhao, J.; Liu, C.; Lu, C. $CO_2$ capture using carbide slag modified by propionic acid in calcium looping process for hydrogen production. *Int. J. Hydrogen Energy* **2013**, *38*, 13655–13663.

28. Gadikota, G.; Zhang, F.; Allen, A. J. Towards understanding the microstructural and

structural changes in natural hierarchical materials for energy recovery: In-operando multi-scale X-ray scattering characterization of Na- and Ca-montmorillonite on heating to 1150 °C. *Fuel* **2017**, *196*, 195–209.

29. Gadikota, G.; Zhang, F.; Allen, A. In Situ angstrom-to-micrometer characterization of the structural and microstructural changes in kaolinite on heating using ultra small-angle, small-angle, and wide-angle X-ray scattering (USAXS/SAXS/WAXS). *Ind. Eng. Chem. Res.* **2017**, *56*, 11791-11801.

30. Gadikota, G.; Allen, A. J. Microstructural and structural characterization of materials for $CO_2$ storage using multi-scale X-ray scattering methods. In Materials and processes for $CO_2$ capture, conversion, and sequestration. Wiley Books, **2017**, *27*, 296-318.

31. Anovitz, L; Cole, D. Characterization and analysis of porosity and pore structures. *Reviews in Mineralogy and Geochemistry,* **2015**, *80*, 61-164.

32. Ilavsky, J.; Zhang, F.; Andrews, R. N.; Kuzmenko, I.; Jemian, P. R.; Levine, L. E.; Allen, A. J. Development of combined microstructure and structure characterization facility for in situ and operando studies at the advanced photon source. *J. Appl. Crystallogr.* **2018**, *51*, 867-882.

33. Benedetti, A.; Ilavsky, J.; Segre, C.; Strumendo, M. Analysis of textural properties of CaO-based $CO_2$ sorbents by ex situ USAXS. *Chem. Eng. J.* **2019**, *355*, 760–776.

34. Chupas, P. J.; Chapman, K. W.; Kurtz, C.; Hanson, J. C.; Lee, P. L.; Grey, C. P. A versatile sample-environment cell for non-ambient X-ray scattering experiments. *J. Appl. Crystallogr.* **2008**, *41*, 822-824.

35. Ilavsky, J.; Jemian, P. R.; Allen, A. J.; Zhang, F.; Levine, L. E.; Long, G. G. Ultra-small-angle X-ray scattering at the Advanced Photon Source. *J. Appl. Crystallogr.* **2009**, *42*, 469–

479.

36. Ilavsky, J.; Zhang, F.; Allen, A. J.; Levine, L. E.; Jemian, P. R.; Long, G. G. Ultra-small-angle X-ray scattering instrument at the advanced photon source: History, recent development, and current status. *Metall. Mater. Trans. A Phys. Metall. Mater. Sci.* **2013**, *44*, 68-76.

37. Black, D. R.; Windover, D.; Henins, A.; Gil, D.; Filliben, J.; Cline, J. P. Certification of NIST standard reference material 640d. *Powder Diffr.* **2010**, *25*, 187–190.

38. Ilavsky, J.; Jemian, P. R. Irena: Tool suite for modeling and analysis of small-angle scattering. *J. Appl. Crystallogr.* **2009**, *42*, 347–353.

39. Ilavsky, J. Nika: Software for two-dimensional data reduction. *J. Appl. Crystallogr.* **2012**, *45*, 324–328.

40. Petch, H. E. The hydrogen positions in portlandite, Ca (OH) 2, as indicated by the electron distribution. *Acta Crystallogr.* **1961**, *14*, 950–957.

41. Gadikota, G.; Zhang, F.; Allen, A. In Situ Angstrom-to-Micrometer Characterization of the Structural and Microstructural Changes in Kaolinite on Heating Using Ultrasmall-Angle, Small-Angle, and Wide-Angle X-ray Scattering (USAXS/SAXS/WAXS). *Ind. Eng. Chem. Res.* **2017**, *56*, 11791-11801.

42. Materic, V.; Smedley, S. I. High Temperature Carbonation of $Ca(OH)_2$. *Ind. Eng. Chem. Res.* **2011**, *50*, 5927–5932.

43. Nikulshina, V.; Gálvez, M. E.; Steinfeld, A. Kinetic analysis of the carbonation reactions for the capture of $CO_2$ from air via the $Ca(OH)_2$-$CaCO_3$-CaO solar thermochemical cycle. *Chem. Eng. J.* **2007**, *129*, 75–83.

44. Kamhi, S. R. On the structure of vaterite, $CaCO_3$. *Acta Crystallogr.* **1963**, *16*, 770–772.

45. Dal Negro, A.; Ungaretti, L. Refinement of the Crystal Structure of Aragonite. *Am. Mineral.* **1971**, *56*, 768–772.

46. Chessin, H.; Hamilton, W. C.; Post, B. Position and thermal parameters of oxygen atoms in calcite. *Acta Crystallogr.* **1965**, *18*, 689–693.

47. Christy, A. G. A review of the structures of vaterite: the impossible, the possible, and the likely. *Cryst. Growth Des.* **2017**, *17*, 3567–3578.

48. Richards, R.; Li, W.; Decker, S.; Davidson, C.; Koper, O.; Zaikovski, V.; Volodin, A.; Rieker, T.; Klabunde, K. J. Consolidation of metal oxide nanocrystals. Reactive pellets with controllable pore structure that represent a new family of porous, inorganic materials. *J. Am. Chem. Soc.* **2000**, *122*, 4921-4925.

49. Liang, J. Z.; Duan, D. R.; Tang, C. Y.; Tsui, C. P. Correlation between impact strength and fractal dimensions of fracture surface for PLLA/nano-$CaCO_3$ composites. *Polym. Test.* **2014**, *35*, 109-115.

50. Diamond, S. Aspects of concrete porosity revisited. *Cem. Concr. Res.* **1999**, *29*, 1181-1188.

51. Liu, M.; Gadikota, G. Probing the Influence of Thermally Induced Structural Changes on the Microstructural Evolution in Shale using Multiscale X-ray Scattering Measurements. *Energy & Fuels* **2018**, *32*, 8193–8201.

52. Fenter, P.; Geissbühler, P.; Dimasi, E.; Srajer, G.; Sorensen, L. B.; Sturchio, N. C. Surface speciation of calcite observed in situ by high-resolution X-ray reflectivity. *Geochim. Cosmochim. Acta* **2000**, *64*, 1221–1228.

53. Maslen, E. N.; Streltsov, V. A.; Streltsova, N. R. X-ray study of the electron density in calcite, $CaCO_3$. *Acta Crystallogr. Sect. B* **1993**, *49*, 636–641.

Peer-reviewed version available at Geosciences 2018, 8, 445; doi:10.3390/geosciences8120445

**Captions for Figures**

**Figure 1.** The cumulative pore volume (a) and pore volume distribution (b) of unreacted calcium hydroxide using BET measurements.

**Figure 2**. Changes in the characteristic peak of calcium hydroxide ($d$ = 3.105 Å, $q$ = 2.024 Å$^{-1}$, h k l: (1 0 0)) and the integrated peak intensity are represented in (a) and (b) respectively [40]. The relative integrated intensity of calcium hydroxide represented in (b) is the integrated intensity of the characteristic peak at a given temperature normalized to the integrated intensity at 30 °C. Vertical bars in (b) represent estimated 5% standard deviation uncertainties.

**Figure 3**. Changes in the characteristic carbonates peaks: calcite ($d$ = 3.85 Å, $q$ = 1.63 Å$^{-1}$, h k l: (0 1 2)) [46] in (a-1), vaterite ($d$ = 2,08 Å, $q$ = 3.02 Å$^{-1}$, h k l: (1 1 0)) [44] in (b-1), and aragonite ($d$ = 2.48 Å, $q$ = 2.53 Å$^{-1}$, h k l: (2 1 0)) [45] in (c-1) as calcium hydroxide is reacted with $CO_2$ at reaction temperatures in the range of 30 °C to 500 °C. The integrated peak intensities of calcite, vaterite, and aragonite are shown in Figures (a-2), (b-2), and (c-2) respectively. Vertical bars represent estimated 5% standard deviation uncertainties in Figures (a-2), (b-2), and (c-2).

**Figure 4.** Identification of the characteristic peaks in unreacted and reacted calcium hydroxide at 30 °C and 497 °C, respectively, using Wide Angle X-Ray Scattering (WAXS) measurements. Peak identification is based on the crystallographic data reported for calcium hydroxide [40], calcite [46,53], vaterite [44,47], and aragonite [45].

**Figure 5**. Changes in the combined slit-smeared USAXS/SAXS data as calcium hydroxide is reacted with $CO_2$ where (a) and (b) represent temperatures in the range of 29 °C to 300 °C and 325 °C to 502 °C, respectively.

**Figure 6.** Porod slopes as calcium hydroxide is reacted with calcium carbonate are represented. Low $q$ and high $q$ ranges represent 0.001-0.01 Å$^{-1}$ and 0.01-0.1 Å$^{-1}$, respectively. The data was

obtained after desmearing the USAXS/SAXS data shown in Figure 5. Porod slope of 1 and 4 indicated scattering from rigid rods and smooth surfaces, respectively. Porod slopes in the range of 2-3 and 3-4 are indicative of branched systems or networks also known as mass fractals and rough interfaces with a fractal dimension, $D$ where $n = 6 - D$ represents a surface fractal.

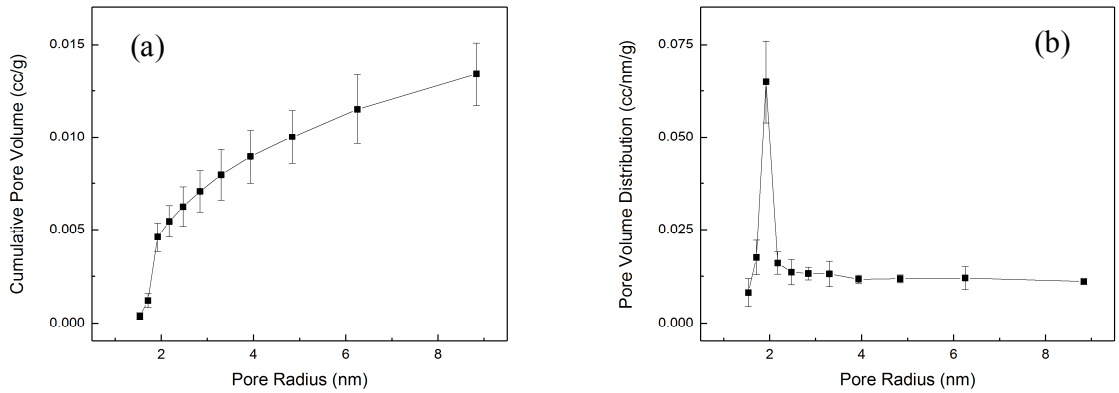


**Figure 1.** The cumulative pore volume (a) and pore volume distribution (b) of unreacted calcium hydroxide using BET measurements.

Preprints (www.preprints.org) | NOT PEER-REVIEWED | Posted: 22 October 2018 doi:10.20944/preprints201810.0476.v1

Peer-reviewed version available at Geosciences 2018, 8, 445; doi:10.3390/geosciences8120445

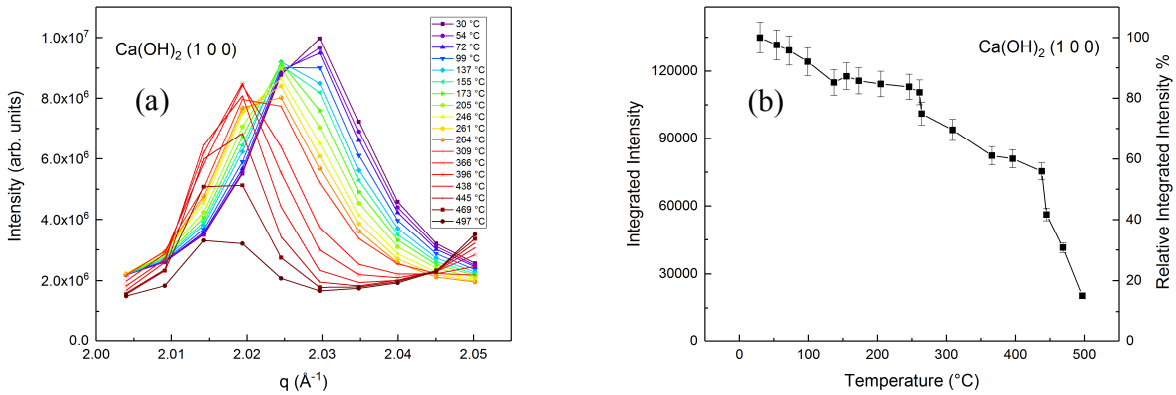


**Figure 2**. Changes in the characteristic peak of calcium hydroxide ($d$ = 3.105 Å, $q$ = 2.024 Å$^{-1}$, h k l: (1 0 0)) and the integrated peak intensity are represented in (a) and (b) respectively [40]. The relative integrated intensity of calcium hydroxide represented in (b) is the integrated intensity of the characteristic peak at a given temperature normalized to the integrated intensity at 30 °C. Vertical bars in (b) represent estimated 5% standard deviation uncertainties.

Preprints (www.preprints.org) | NOT PEER-REVIEWED | Posted: 22 October 2018 doi:10.20944/preprints201810.0476.v1

Peer-reviewed version available at Geosciences 2018, 8, 445; doi:10.3390/geosciences8120445

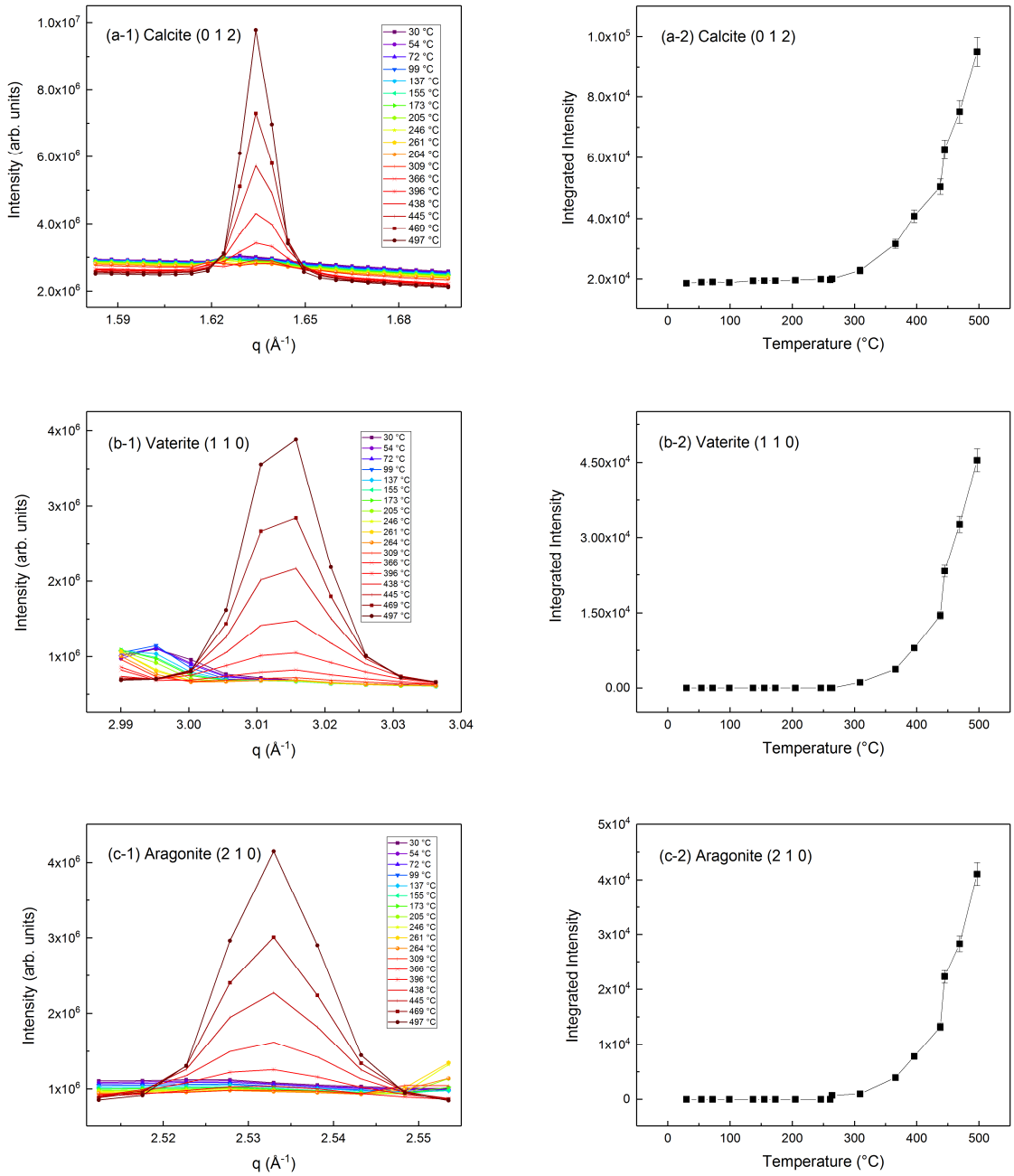


**Figure 3**. Changes in the characteristic carbonates peaks: calcite ($d$ = 3.85 Å, $q$ = 1.63 Å$^{-1}$, h k l: (0 1 2)) [46] in (a-1), vaterite ($d$ = 2,08 Å, $q$ = 3.02 Å$^{-1}$, h k l: (1 1 0)) [44] in (b-1), and aragonite ($d$ = 2.48 Å, $q$ = 2.53 Å$^{-1}$, h k l: (2 1 0)) [45] in (c-1) as calcium hydroxide is reacted with $CO_2$ at reaction temperatures in the range of 30 °C to 500 °C. The integrated peak intensities of calcite,

1 vaterite, and aragonite are shown in Figures (a-2), (b-2), and (c-2) respectively. Vertical bars
2 represent estimated 5% standard deviation uncertainties in Figures (a-2), (b-2), and (c-2).

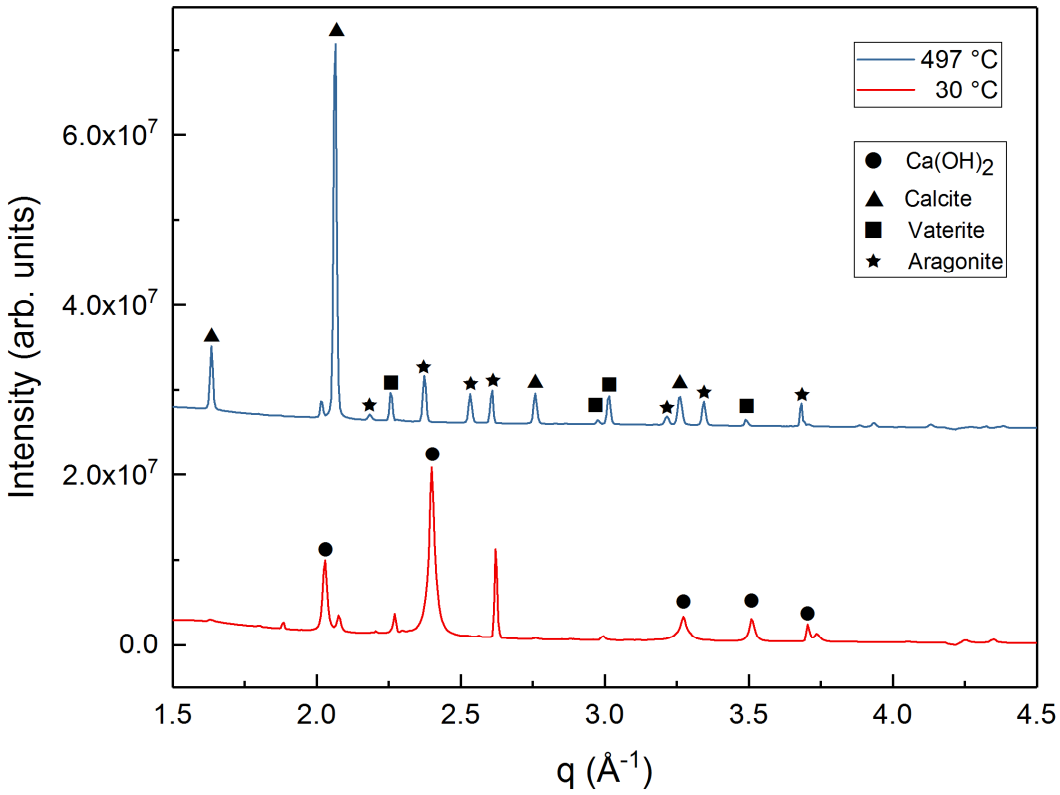


**Figure 4.** Identification of the characteristic peaks in unreacted and reacted calcium hydroxide at 30 °C and 497 °C, respectively, using Wide Angle X-Ray Scattering (WAXS) measurements. Peak identification is based on the crystallographic data reported for calcium hydroxide [40], calcite [46,53], vaterite [44,47], and aragonite [45].

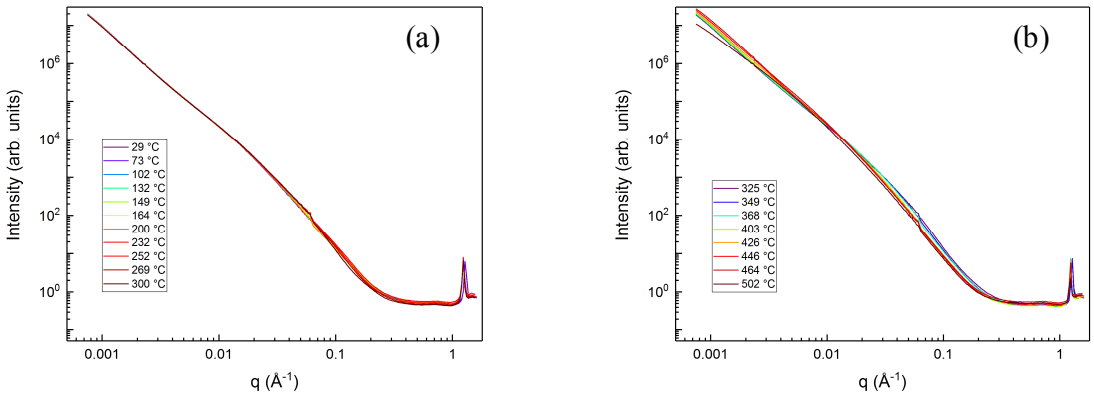


**Figure 5**. Changes in the combined slit-smeared USAXS/SAXS data as calcium hydroxide is reacted with $CO_2$ where (a) and (b) represent temperatures in the range of 29 °C to 300 °C and 325 °C to 502 °C, respectively.

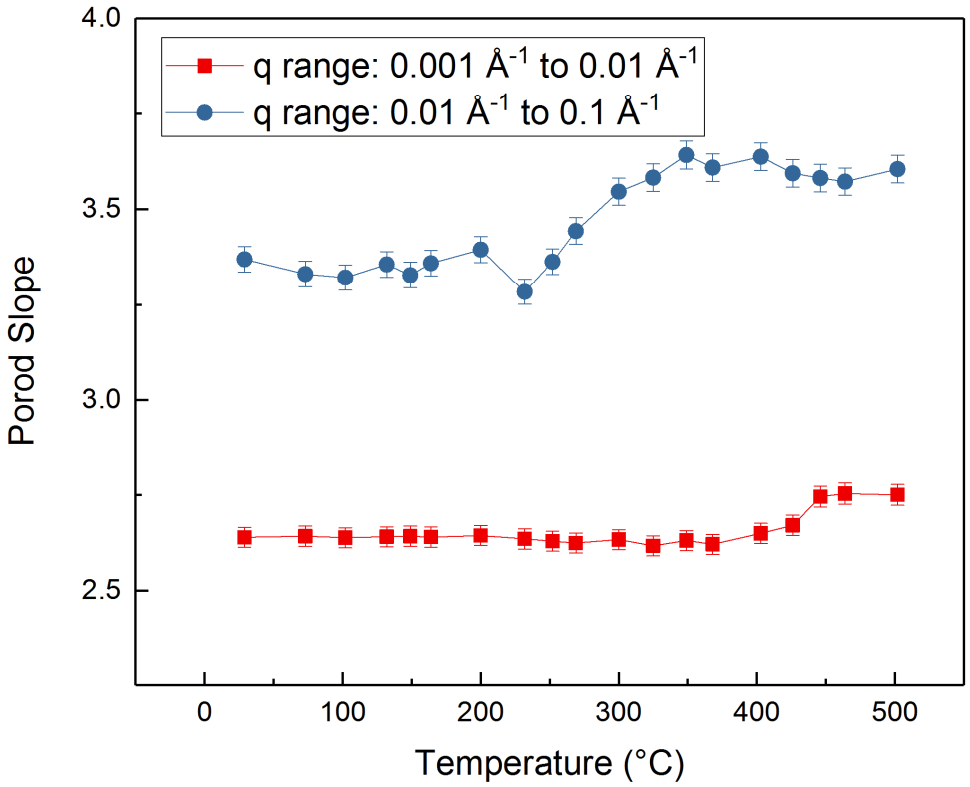


**Figure 6.** Porod slopes as calcium hydroxide is reacted with calcium carbonate are represented. Low *q* and high *q* ranges represent 0.001-0.01 Å$^{-1}$ and 0.01-0.1 Å$^{-1}$, respectively. The data was obtained after desmearing the USAXS/SAXS data shown in Figure 5. Porod slope of 1 and 4 indicated scattering from rigid rods and smooth surfaces, respectively. Porod slopes in the range of 2-3 and 3-4 are indicative of branched systems or networks also known as mass fractals and rough interfaces with a fractal dimension, *D* where $n = 6 - D$ represents a surface fractal.